

# 1 Quantifying vegetation indices using Terrestrial Laser 2 Scanning: methodological complexities and ecological insights 3 from a Mediterranean forest

4 William Rupert Moore Flynn<sup>1</sup>, Harry Jon Foord Owen<sup>2</sup>, Stuart William David Grieve<sup>1,3</sup> and  
5 Emily Rebecca Lines<sup>2</sup>

6 <sup>1</sup>School of Geography, Queen Mary University of London, Mile End Rd, Bethnal Green, London E1 4NS

7 <sup>2</sup>Department of Geography, University of Cambridge, Downing Place, Cambridge, CB2 3EN

8 <sup>3</sup>Digital Environment Research Institute, Queen Mary University of London, New Road, London, E1 1HH

9 Correspondence to: W. R. M. Flynn ([w.r.m.flynn@qmul.ac.uk](mailto:w.r.m.flynn@qmul.ac.uk))

10 **Abstract.** Accurate measurement of vegetation density metrics including plant, wood and leaf area indices (PAI,  
11 WAI and LAI) is key to monitoring and modelling carbon storage and uptake in forests. Traditional passive sensor  
12 approaches, such as Digital Hemispherical Photography (DHP), cannot separate leaf and wood material, nor  
13 individual trees, and require many assumptions in processing. Terrestrial Laser Scanning (TLS) data offer new  
14 opportunities to improve understanding of tree and canopy structure. Multiple methods have been developed to  
15 derive PAI and LAI from TLS data, but there is little consensus on the best approach, nor are methods  
16 benchmarked as standard.

17 Using TLS data collected in 33 plots containing 2472 trees of five species in Mediterranean forests, we compare  
18 three TLS methods (*LiDAR Pulse*, *2D Intensity Image* and *Voxel-Based*) to derive PAI and compare with co-  
19 located DHP. We then separate leaf and wood in individual tree point clouds to calculate the ratio of wood to total  
20 plant area ( $\alpha$ ), a metric to correct for non-photosynthetic material in LAI estimates. We use individual tree TLS  
21 point clouds to estimate how  $\alpha$  varies with species, tree height and stand density.

22 We find the *LiDAR Pulse* method agrees most closely with DHP, but is limited to single scan data so cannot  
23 determine individual tree properties, including  $\alpha$ . The *Voxel-Based* method shows promise for ecological studies  
24 as it can be applied to individual tree point clouds. Using the *Voxel-Based* method, we show that species explain  
25 some variation in  $\alpha$ , however, height and plot density were ~~stronger~~ better predictors.

26 Our findings highlight the value of TLS data to improve fundamental understanding of tree form and function,  
27 but also the importance of rigorous testing of TLS data processing methods at a time when new approaches are  
28 being rapidly developed. New algorithms need to be compared against traditional methods, and existing  
29 algorithms, using common reference data. Whilst promising, our results show that metrics derived from TLS data  
30 are not yet reliably calibrated and validated to the extent they are ready to replace traditional approaches for large  
31 scale monitoring of PAI and LAI.

## 33 1 Introduction

34 Terrestrial Laser Scanning (TLS) generates high-resolution 3D measurements of whole forests and individual  
35 trees (Burt et al., 2018; Disney, 2018), leading to the development of completely new monitoring approaches to  
36 understand the structure and function of ecosystems (Lines et al., 2022). Unlike traditional passive sensors, TLS  
37 can estimate plant, wood and leaf area indices (PAI; WAI; LAI) for both whole plots and individual tree point  
38 clouds (Calders et al., 2018), and is unaffected by illumination conditions. This has led to the development of  
39 several methods for processing TLS data to extract the key metrics PAI, WAI and LAI (e.g. Hosoi and Omasa,  
40 2006; Jupp et al., 2008; Zheng et al., 2013). However, intercomparison studies of algorithms and processing  
41 approaches to derive the same metrics from different TLS methods are lacking.

42 Leaf Area Index (LAI), defined as half the amount of green leaf area per unit ground area (Chen and Black, 1992),  
43 determines global evapotranspiration, phenological patterns and canopy photosynthesis, and is therefore an  
44 essential climate variable (ECV), as well as a key input in dynamic global vegetation models (Sea et al., 2011;  
45 Weiss et al., 2004). Accurate measurements of LAI, WAI and PAI have historically been derived from labour  
46 intensive destructive sampling (Baret et al., 2013; Jonckheere et al., 2004), so over large spatial or temporal scales  
47 these can only be measured indirectly, typically with remote sensing. Large-scale remote sensing, using  
48 spaceborne and airborne instruments, has been widely used to estimate LAI over large areas (Pfeifer et al., 2012),  
49 but requires calibration and validation using in situ measurements to constrain information retrieval (Calders et  
50 al., 2018). Non-destructive in situ vegetation index estimates have historically been made by measuring light  
51 transmission below the canopy and using simplifying assumptions about canopy structure to estimate the amount  
52 of intercepting material (e.g. Beer-Lambert law; Monsi and Saeki, 1953). The most common method, Digital  
53 Hemispherical Photography (DHP; Figure 1a), requires both model assumptions and subjective user choices  
54 during data acquisition and processing in order to estimate both PAI and LAI (Breda, 2003). DHP images are  
55 processed by separating sky from canopy, but not photosynthetic from non-photosynthetic vegetative material, so  
56 additional assumptions are needed to calculate either LAI or WAI (Jonckheere et al., 2004; Pfeifer et al., 2012).  
57 Separation of LAI from PAI can be achieved by removing or masking branches and stems from hemispherical  
58 images (e.g. Sea et al., 2011; Woodgate et al., 2016), but is not reliable when leaves are occluded by woody  
59 components (Hardwick et al., 2015). An alternative approach is to take separate DHP measurements in both leaf  
60 on and leaf off conditions, and derive empirical wood to plant ratios (WAI/PAI,  $\alpha$ ) (Leblanc and Chen, 2001), but  
61 this is not always practical, for example in evergreen forests. The difficulty of separation means that studies often  
62 omit correcting for the effect of WAI on optical PAI measurements altogether (Woodgate et al., 2016), but since  
63 woody components in the forest canopy can account for more than 30% of PAI (Ma et al., 2016) this can introduce  
64 overestimation. Further, although DHP estimates of LAI or PAI are valuable both for ecosystem monitoring and  
65 developing satellite LAI products (Hardwick et al., 2015; Pfeifer et al., 2012), they are limited to sampling only  
66 at a neighbourhood or plot level (Weiss et al., 2004), and cannot be used to measure individual tree LAI except  
67 for open grown trees (Béland et al., 2014).

68 The ratio of wood to total plant area,  $\alpha$ , is known to be dynamic, changing in response to abiotic and biotic  
69 conditions. For example, the Huber value (sapwood to leaf area ratio, a related measure to  $\alpha$ ) may vary according  
70 to water availability (Carter and White 2009). Leaf area may therefore be indicative of the drought tolerance level  
71 of a tree, with more drought tolerant species displaying a lower leaf area, reducing the hydraulic conductance of

72 the whole tree and therefore increasing its drought tolerance (Niinemets and Valladares, 2006).  $\alpha$  has been  
73 hypothesised to increase with the size of a tree in response to the increased hydraulic demand associated with  
74 greater hydraulic resistance of tall trees (Magnani et al., 2000) and higher transpiration rates of larger LAI  
75 (Battaglia et al., 1998; Phillips et al., 2003). Stand density may also impact  $\alpha$  (Long and Smith, 1988; Whitehead,  
76 1978), as increased stand level water use scales linearly with LAI (Battaglia et al., 1998; Specht and Specht, 1989),  
77 reducing water availability to individual trees competing for the same resources (Jump et al., 2017). Large scale  
78 quantification of  $\alpha$  or Huber value, however, is difficult as studies usually rely on a small number of destructively  
79 sampled trees (e.g. Carter and White, 2009; Magnani et al., 2000), litterfall traps (e.g. Phillips et al., 2003) or  
80 masking hemispherical images (e.g. Sea et al., 2011; Woodgate et al., 2016). These approaches are only applicable  
81 on a small to medium scale, and in the case of image masking, cannot differentiate between individuals. Variation  
82 in  $\alpha$ , for example by species and or stand structure, is therefore largely unknown.

### 83 1.2 TLS methods for calculating PAI, LAI and WAI

84 TLS methods for extracting PAI, LAI and WAI can be broadly categorised into two types: (1) LiDAR return  
85 counting, using single scan data (e.g., the *LiDAR Pulse* method; Jupp et al., 2008, and *2D Intensity Image* method;  
86 Zheng et al., 2013) and (2) point cloud voxelisation, usually using co-registered scans (e.g., the *Voxel-Based*  
87 method; Hosoi and Omasa, 2006).

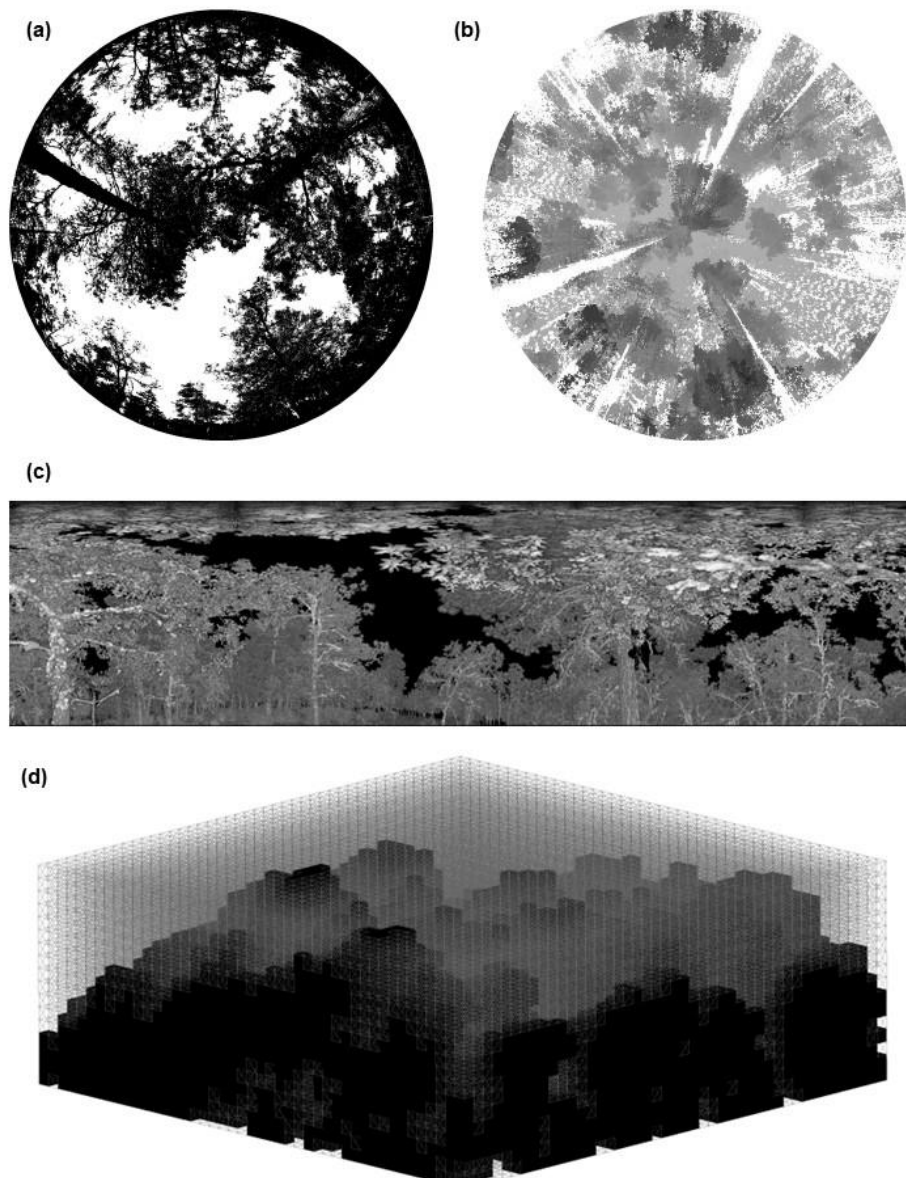
88 The *LiDAR Pulse* method (Jupp et al., 2008; Figure 1b) estimates gap fraction ( $P_{gap}$ ) using single scan data,  
89 as a function of the total number of outgoing LiDAR pulses from the sensor and the number of pulses that are  
90 intercepted by the canopy. This method, which eliminates illumination impacts associated with the use of DHP  
91 (Calders et al., 2014), has been implemented in the python module, *PyLidar* ([www.pylidar.org](http://www.pylidar.org)) and the R package,  
92 *rTLS* (Guzman, et al. 2021). Using the *LiDAR Pulse* method, Calderys et al. (2018) compared TLS-PAI-PAI  
93 estimates from two ground-based passive sensors (LiCOR LAI-2000 and DHP) with TLS data collected with a  
94 RIEGL VZ-400 TLS in a deciduous woodland, and found the two passive sensors underestimated PAI values  
95 compared to TLS, with differences dependent on DHP processing and leaf on/off conditions.

96 The *2D Intensity Image* method (Zheng et al., 2013; Figure 1c), also uses raw single scan TLS point clouds, but,  
97 unlike the *LiDAR Pulse* method, ~~this approach~~ converts LiDAR returns into 2D panoramas where pixel values  
98 represent return intensity. PAI is estimated by classifying pixels as sky or vegetation, based on their intensity  
99 value, to estimate  $P_{gap}$ , and then applying Beer-Lambert's law. ~~As for~~ Like the *LiDAR Pulse* method, this  
100 approach has been shown to generate higher PAI estimates than DHP (Calderys et al., 2018; Woodgate et al., 2015;  
101 Grotti et al., 2020), with differences attributed to the greater pixel resolution and viewing distance of TLS  
102 resolving more small canopy details (Grotti et al., 2020).

103 The *Voxel-Based* method (Figure 1d) estimates PAI by segmenting a point cloud into voxels and either simulating  
104 radiative transfer within each cube (Béland et al., 2014; Kamoske et al., 2019), or classifying voxels as either  
105 containing vegetation or not, and dividing vegetation voxels by the total number of voxels (Hosoi and Omasa,  
106 2006; Itakura and Hosoi, 2019; Li et al., 2017). Crucially, this method may be applied to multiple co-registered  
107 scan point clouds and so can be used to calculate PAI for both whole plots and individual, segmented TLS trees.  
108 However, PAI estimates derived using the voxel method are highly dependent on voxel size (Calderys et al., 2020).  
109 Using a radiative transfer approach, Béland et al., (2014) demonstrated that voxel size is dependent on canopy

110 clumping, radiative transfer model assumptions and occlusion effects, making a single, fixed choice of voxel size  
111 for all ecosystem types, scanners or datasets impossible. To test various approaches to selecting voxel size using  
112 a voxel classification approach, (Li et al., (2016) matched voxel size to point cloud resolution, individual tree leaf  
113 size, and minimum beam distance and tested against destructive samples, finding that voxel size matched to point  
114 cloud resolution had the closest PAI values to destructive samples.

115 The *LiDAR Pulse* method and *2D Intensity Image* method both use single scan data. However, to generate robust  
116 estimates of canopy properties that avoid errors from occlusion effects, multiple co-registered scans taken from  
117 different locations are likely needed (Wilkes et al., 2017). Further, both these methods require raw unfiltered data  
118 to accurately measure the ratio of pulses emitted from the scanner and number of pulses that are intercepted by  
119 vegetation. This means “noisy” points caused by backscattered pulses (Wilkes et al., 2017) are included in  
120 analyses, potentially leading to higher PAI estimates. However, the *LiDAR Pulse* and *2D Intensity Image* methods  
121 may introduce fewer estimation errors compared to DHP, which is influenced by differences in sky illumination  
122 conditions and camera exposure (Weiss et al., 2004).



125 **Figure 1: Visual representation of the four Methods for PAI and WAI estimation applied-used in this study: (a) a**  
 126 **binarised digital hemispherical photograph (DHP), (b) TLS raw single scan point cloud, ~~used within for~~ the *LiDAR***  
 127 ***Pulse* method (Jupp et al., 2008). Image shows a top-down view of raw point cloud and greyscale represents low (grey)**  
 128 **and high (black) Z values, (c) TLS 2D intensity image for the *2D Intensity Image* method (Zheng et al., 2013), (d)**  
 129 **Voxelised co-registered whole plot point cloud for the *Voxel-Based* method (Hosoi and Omasa, 2006), showing a**  
 130 **representative schematic of cube voxels with edge length of 1m, voxelised using the *R* package *VoxR* (Lecigne et al.,**  
 131 **2018). Solid black voxels are classified as containing vegetation (filled) and voxels outlined with grey lines are voxels**  
 132 **classified as empty.**

### 133 1.3 Scope and aims

134 The aims of this study are twofold: the first aim is to compare three TLS methods for estimating PAI with  
 135 traditional DHP. The second aim of this study is to use TLS to understand drivers of individual tree  $\alpha$  variation.

136 In this study we use a dataset of 528 co-located DHP and high-resolution TLS scans from 33 forest plots to  
 137 compare DHP derived PAI ( $PAI_{DHP}$ ) with estimates from three methods to estimate PAI from TLS data ( $PAI_{TLS}$ ):  
 138 the *LiDAR Pulse* method; the *2D Intensity Image* method and the *Voxel-Based* method (Figure 1). We use a dataset  
 139 collected from a network of pine/oak forest plots in Spain (Owen et al., 2021) and ask (1) are the three TLS  
 140 methods able to reproduce  $DHP-PAI/PAI_{DHP}$  estimates at single scan and whole plot level? (2) does  $\alpha$ , calculated  
 141 from the *Voxel-Based* method on individual tree point clouds, vary with species and tolerance to drought? and (3)  
 142 does  $\alpha$  scale with height and stand density?

## 143 2. Methods

### 144 2.1 Study site

145 We collected TLS and DHP data from 29 plots in Alto Tajo Natural Park ([40°41'N 02°03'W](#); FunDIV – Functional  
 146 Diversity plots; see Baeten et al., (2013) for a detailed description of the plots) and four plots in Cuellar  
 147 ([41°23'N 4°21'W](#)) in June - July 2018 (see Owen et al., (2021) for full details) (Figure A1). Plots contained two  
 148 oak species: semi-deciduous *Q. faginea* and evergreen *Q. ilex*, and three pine species: *P. nigra*, *P. pinaster* and *P.*  
 149 *sylvestris*. *P. sylvestris* is the least drought tolerant species, followed by *P. nigra*, *Q. faginea*, *Q. ilex*; shade  
 150 tolerance follows the same ranking (Niinemets and Valladares, 2006; Owen et al., 2021). Although not  
 151 quantitatively ranked, *P. pinaster* has been shown to be very drought tolerant, appearing in drier areas than the  
 152 other species (Madrigal-González et al., 2017). The area is characterised by a Mediterranean climate (altitudinal  
 153 gradient range 840 – 1400 m.a.s.l.) (Jucker et al., 2014; Madrigal-González et al., 2017). In addition to the five  
 154 main canopy tree species, plots contained an understory of *Juniperus thurifera* and *Buxus sempervirens* (Kuusk  
 155 et al., 2018).

### 156 2.2 Field protocol

157 In each of the 33 30 x 30 m plots we collected TLS scans on a 10 m grid, making 16 scan locations following  
 158 Wilkes et al., (2017) to minimise occlusion effects associated with insufficient scans. We used a Leica HDS6200  
 159 TLS set to super high resolution (3.1 x 3.1mm resolution at 10 m with a beam divergence of  $\leq 5$  mm at 50 m; scan  
 160 time 6m 44 s; see Owen et al., (2021)). At each of the 528 scan locations and following the protocol in Pfeifer et  
 161 al., (2012), we captured co-located DHP images with three exposure settings (automatic and  $\pm$  one stop exposure  
 162 compensation), levelling a Canon EOS 6D full frame DSLR sensor with a Sigma EX DG F3.5 fisheye lens,  
 163 mounted on a Vanguard Alta Pro 263AT tripod.



### 164 2.3 Calculation of single scan and whole plot PAI using DHP data

165 For each of the red-green-blue (RGB) DHP images we extracted the blue band for image thresholding, as this best  
166 represents sky/vegetation contrast (Pfeifer et al., 2012). For each plot, we picked the exposure setting that best  
167 represented sky/vegetation difference based on pixel brightness histograms of four sample locations indicative of  
168 the plot. We carried out automatic image thresholding using the Ridler and Calvard method (1978), to create a  
169 binary image of sky and vegetation, avoiding subjective user pixel classification (Jonckheere et al., 2005). We  
170 calculated PAI from the binary image, limiting the field of view to a  $5^\circ$  band centred on the hinge angle of  $57.5^\circ$   
171 ( $55^\circ - 60^\circ$ ). The hinge angle has a path length through the canopy twice the canopy height, so the band around it  
172 is an area of significant spatial averaging taken as representative of canopy structure of the area (Calders et al.,  
173 2018; Jupp et al., 2008). From the binarised hinge angle band we calculated ~~gap fraction~~  $P_{gap}$  as the number of sky  
174 pixels divided by the total number of pixels and PAI using an inverse Beer-Lambert law equation (Monsi and  
175 Saeki, 1953). We calculated whole plot PAI as the arithmetic mean ~~of the 16 within~~ plot scan location PAI  
176 estimates. As this value does not correct for canopy clumping, it is better described as effective PAI, rather than  
177 true PAI (Woodgate et al., 2015). However, as the TLS and DHP methods we apply here account for canopy  
178 clumping differently, we compare effective values and here-on refer to effective PAI as PAI (Calders et al.,  
179 2018). DHP images used in this study are freely available (see Flynn et al., 2023).

### 180 2.4 Calculation of single scan and whole plot PAI from TLS data

181 To calculate PAI using the *LiDAR Pulse* method (Jupp et al., 2008), we calculated ~~the gap fraction~~ ( $P_{gap}$ ) for a  
182 single scan (Figure 1b) by summing all returned laser pulses and dividing by the number of total outgoing pulses,  
183 following Lovell et al. (2011; see Eq. 7 in that study), and then estimated PAI following Jupp et al. (2008; see Eq.  
184 18 in that study), setting the sensor range to  $5^\circ$  around the hinge angle as before ( $55^\circ - 60^\circ$ ). Single scan PAI was  
185 taken as the cumulative sum of PAI values estimated by vertically dividing the hinge region into 25 cm intervals  
186 (Calders et al., 2014). We implemented the *LiDAR Pulse* method using the open-source *R* (R Core Team, 2020)  
187 package, *rTLS* (Guzmán and Hernandez, 2021).

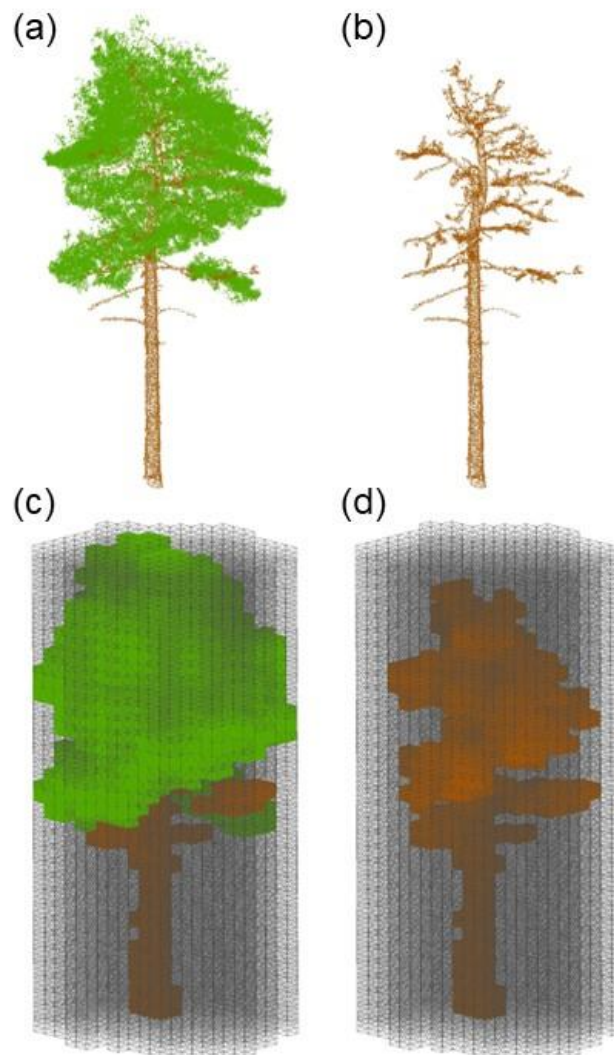
188 To calculate PAI using the *2D Intensity Image* method (Zheng et al., 2013), we converted 3D TLS point cloud  
189 data from all 528 scan locations into polar coordinates, ~~and~~ scaled intensity values to cover the full 0-255 range  
190 (Figure 1c) and rasterised into a 2D intensity image using the open-source *R* package, *raster* (Hijmans, 2022). We  
191 cut the 2D intensity image to a  $5^\circ$  band around the hinge angle ( $55^\circ - 60^\circ$ ) and classified sky and vegetation pixels  
192 in each image using the Ridler and Calvard method (1978). We calculated  $P_{gap}$  as the number of pixels classified  
193 as sky divided by the total number of pixels and derived PAI with an inverse Beer-Lambert law equation (Monsi  
194 and Saeki, 1953).

195 Following the same approach as applied to our DHP data, we calculated whole plot PAI for the *LiDAR Pulse* and  
196 *2D Intensity Image* methods as the arithmetic mean of ~~within the 16~~ plot single-scan location PAI estimates.

197 To calculate PAI using the *Voxel-Based* method, we followed a voxel classification approach (Hosoi and Omasa,  
198 2006), downsampling the point cloud to 0.05 m to aid computation time and matching the voxel size to the  
199 resolution of the point cloud (~~0.05 m~~), following (Li et al., (2016), who showed that matching the voxel size to  
200 the point cloud point to point minimum distance (resolution) increases accuracy as small canopy gaps are not  
201 included in voxels classified as vegetation. We chose to use a voxel classification approach (rather than a radiative

202 transfer based one) as this method is widely applicable to a range of TLS systems and levels of processing, as well  
 203 as providing explicit guidance on voxel size selection, which is known to impact derived PAI estimates (Li et al.,  
 204 2016). We re-combined individually segmented trees, filtered for noise using a height-dependent statistical filter  
 205 (see Owen et al., 2021) back into whole plot point clouds and voxelised them using the open source *R* package,  
 206 *VoxR* (Lecigne et al., 2018), with a full grid covering the minimum to maximum XYZ ranges of the plot. We  
 207 classified any voxel containing  $> 0$  points as vegetation (“filled”), and empty voxels as gaps. We then split the  
 208 voxelised point cloud vertically into slices one voxel high. Within each slice, the contact frequency is calculated  
 209 as the fraction of filled to total number of voxels. We then multiplied the contact frequency by a correction factor  
 210 for leaf inclination, set at 1.1 (Li et al., 2017), and whole plot PAI was calculated as the sum of all slices’ contact  
 211 frequencies.

## 212 2.5 Calculation of individual tree PAI, WAI and $\alpha$ using the voxel-based method



213 **Figure 2: Visualisation of the workflow for applying the Voxel-Based method to estimate individual-tree PAI, WAI and**  
 214  **$\alpha$ .** (a) Individual tree point cloud; (b) separated leaf off (wood) individual tree point cloud; (c) voxelised individual tree  
 215 **point cloud; (d) voxelised wood cloud. Solid black-Coloured voxels (green represents leaf and brown represents wood)**  
 216 **are filled voxels and grey lines are empty voxels. Empty voxels occupy the space within the projected crown area of the**  
 217 **tree. Image shows schematic of point cloud voxelised with cube voxels with edge length of 0.5 m. Panels (a) and (b)**  
 218 **show ~~W~~wood and leaf separation of an example *P. sylvestris*, was carried out using *TLSeparation* (Vicari et al., 2019).**

219 **Point cloud voxelisation was carried out using modified functions from R package VoxR (Lecigne et al., 2018). Note**  
220 **that our method used voxel sizes at the resolution of the cloud (5 cm), but here we present an image with larger voxels**  
221 **to ease visual interpretation.**

222 As the only method using multiple co-registered scans, the *Voxel-Based* method is only method compared in this  
223 study we found capable of deriving PAI, WAI and LAI of segmented individual tree point clouds ~~estimating~~  
224 ~~individual tree leaf and wood properties~~. We estimated PAI and WAI for 2472 individual trees segmented from  
225 co-registered point clouds following a similar method to the whole plot point cloud. We used individual tree point  
226 clouds downsampled to 0.05 m, to aid computation time, and extracted segmented individual trees using the  
227 automated tree segmentation program *treeseq* (Burt et al., 2019), implemented in C++, see by Owen et al., (2021)  
228 for that study, full details, and Individual segmented tree data used in this study are freely available (see Owen et  
229 al., 2022) ~~(Owen et al., 2022), for individual segmented tree data.~~

230 To estimate PAI, WAI and  $\alpha$  for each tree, we ~~first separated leaf from wood points in~~ used individual tree point  
231 clouds wood – leaf separated by ~~(Owen et al., (2021)~~ using the open source Python library *TLSeparation* (Vicari  
232 et al., 2019), and then used the separated wood-~~only~~ point clouds to calculate WAI. *TLSeparation* ~~classifies~~  
233 assigns points ~~as as either~~ leaf or wood, iteratively looking at a predetermined number of nearest neighbours (*knn*).  
234 The *knn* of each iteration is directly dependent on point cloud density, since high density point clouds will require  
235 higher a *knn* (Vicari et al., 2019). ~~We used~~ The utility package in TLSeparation was used to automatically detect  
236 the optimum *knn* for each tree point cloud.

237 To voxelise individual tree complete (Figure 2a) and wood only (Figure 2b) point clouds, we used a modified  
238 approach based on Lecigne et al., (2018), voxelising within the projected crown area of the whole tree point cloud  
239 (Figure 2c) to calculate PAI. In the same way as for PAI, w ~~We~~ calculated WAI using the separated wood point  
240 cloud within the projected crown area of the whole tree (Figure 2d; using the whole crown and not just the wood  
241 point cloud), and derived  $\alpha$  for each tree as  $WAI/P AI$ . allowing a comparison with existing literature estimating  
242  $\alpha$  for a range of ecosystems, (Sea et al., 2011; Woodgate et al., 2016).

## 243 **2.6 Statistical Analyses**

244 We tested the relationships between ~~TLS PAI~~ $PAI_{TLS}$  and ~~DHP PAI~~ $PAI_{DHP}$  estimates using Standardised Major  
245 Axis (SMA) using the open source R (R Core Team, 2020) package, *smatr* (Warton et al., 2012). SMA is an  
246 approach to estimating a line of best fit where we are not able to predict one variable from another (Warton et al.,  
247 2006); we chose SMA because we do not have a ‘true’ validation dataset, so avoid assuming either DHP or any  
248 of the TLS methods produces the most accurate results. For each TLS method, we assessed the relationship with  
249 DHP using the coefficient of determination and RMSE. We chose to compare PAI values rather than WAI or LAI  
250 as to do so would mean an additional correction for non-photosynthetic elements, which each method does in  
251 different ways, so introducing further source of uncertainty and limiting our ability to fairly compare processing  
252 approaches. To further understand observed drivers of variance in PAI, we tested the relationship between PAI  
253 and ~~TLS estimated~~ whole plot crown area index, CAI, a proxy measure of stand density and local competition  
254 (Caspersen et al., 2011; Coomes et al., 2012). We calculated CAI as the sum of TLS-derived projected crown  
255 area, divided by the plot area (Owen et al., 2021), and indicative measure of stand density, using SMA.

256



257 To test if  $\alpha$  differs by species, we used linear mixed models (LMMs) in the *R* package, *lme4* (Bates et al., 2015).  
258 We included an intercept only random plot effect to account for local effects on  $\alpha$ :

259

$$260 \quad \alpha_{i,sj} = a_s + Plot_j \quad (1)$$

261

262 here,  $\alpha_i$  is  $\alpha$  of an individual of species  $s$ , in plot  $j$ , and  $a_s$  is the parameter to be fit. To test the effect of stand  
263 structure and tree height on  $\alpha$ , we fit relationships separately for each species, again including a random plot  
264 effect:

265

$$266 \quad \alpha_{i,sj} = a_s + b_s H_i + c_s CAI_j + Plot_{sj} \quad (2)$$

267

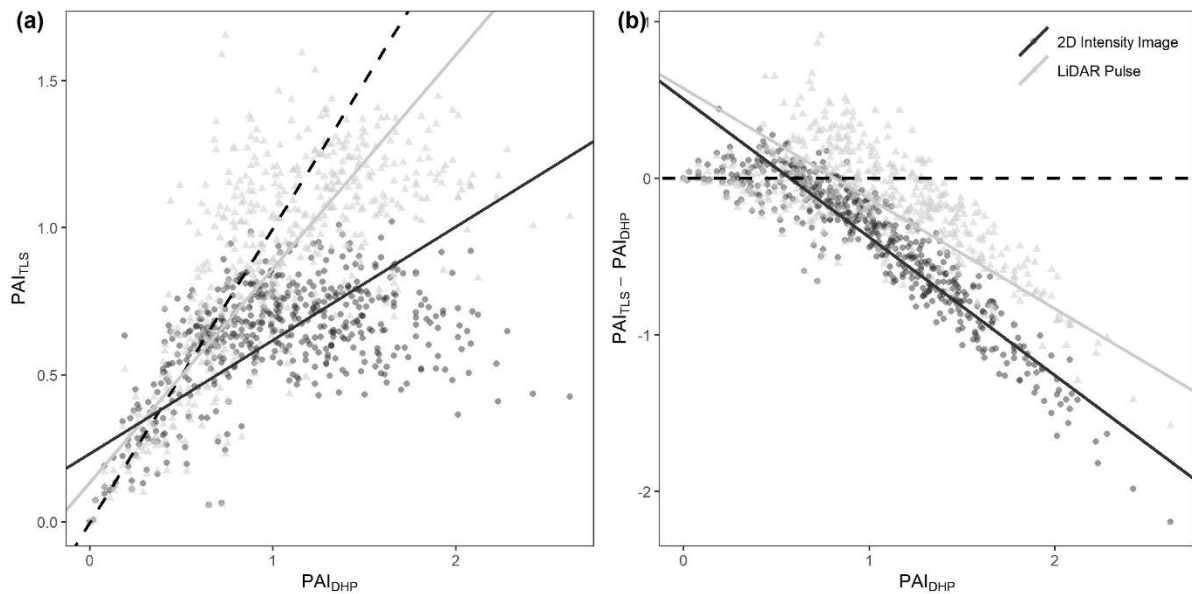
268 here  $H_i$  is the height of the tree,  $CAI_j$  is the crown area index for the plot, with other parameters as before.

269 For each species' model (equation 2), we calculated the intra-class correlation coefficient (ICC). The ICC, similar  
270 to coefficient of determination, quantifies the amount of variance explained by the random effect in a linear mixed  
271 model (Nakagawa et al., 2017).

### 272 3. Results

#### 273 3.1 Comparison of plant area index estimated by DHP and single scan TLS

274 Of the two single scan TLS methods tested (*LiDAR Pulse* method and *2D Intensity Image* method), we found that  
275 ~~the relationship between~~ PAI estimated using the *LiDAR Pulse* method ~~and more strongly agreed with DHP~~  
276 ~~PAI/PAI<sub>DHP</sub>, but there was also significant correlation for~~ ~~had a higher R<sup>2</sup> than~~ the *2D Intensity Image* method  
277 (SMA; *LiDAR Pulse* method R<sup>2</sup> = 0.50, slope = 0.73, p < 0.001, RMSE = 0.14, and *2D Intensity Image* method R<sup>2</sup>  
278 = 0.22, slope = 0.38, p < 0.001, RMSE = 0.39, respectively, Figure 3a). At larger PAI values, both TLS methods  
279 underestimated PAI ~~relative to DHP compared with DHP~~ (Figure 3b). We found statistically significant negative  
280 correlations between residuals and DHP for both methods (SMA; *2D Intensity Image* method residuals R<sup>2</sup> = 0.85,  
281 slope = -0.88, p < 0.01; *LiDAR Pulse* method residuals R<sup>2</sup> = 0.47, slope = -0.70, p < 0.01; Figure 3b). The *2D*  
282 *Intensity Image* method showed larger underestimation at higher ~~DHP PAI/PAI<sub>DHP</sub>~~ values, suggesting this method  
283 may saturate sooner ~~for higher PAI values~~ than ~~either both~~-DHP ~~or and~~ the *LiDAR Pulse* method ~~at higher PAI~~  
284 ~~values~~ (Figure 3b).



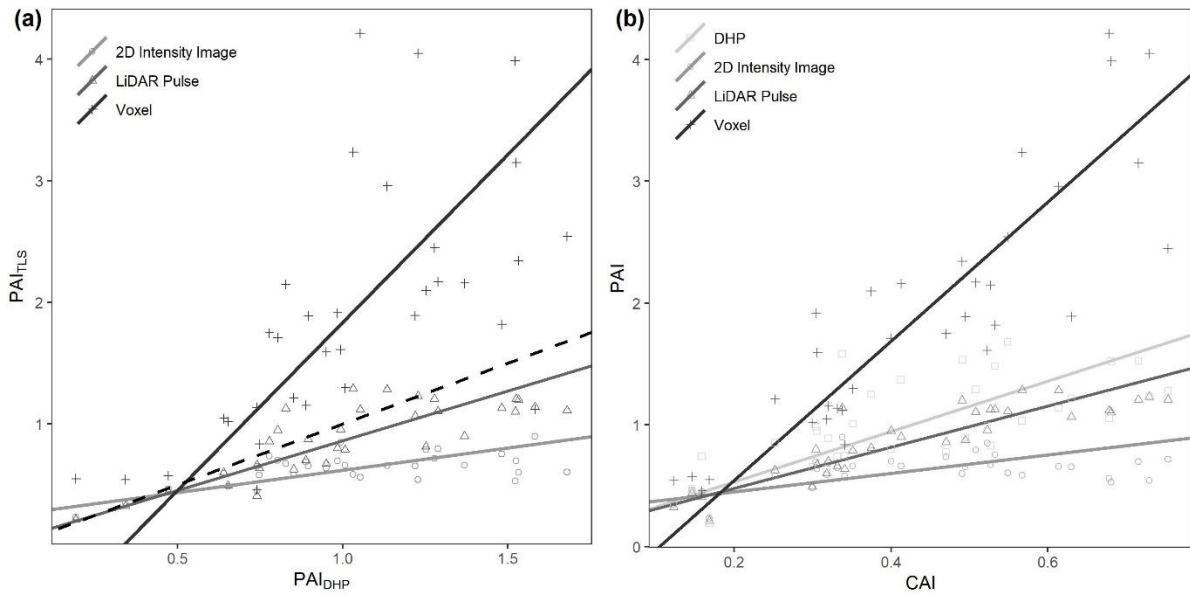
285

286 **Figure 3: Comparison of single scan  $\text{PAI}_{\text{TLS}}$  and  $\text{PAI}_{\text{DHP}}$  estimates, for all 528 scan locations (16 per**  
 287 **plot). (a) The correlation between DHP derived PAI with PAI derived using the 2D Intensity Image method  $R^2 = 0.22$ ,**  
 288 **slope = 0.38,  $p < 0.001$ , RMSE = 0.39 (circles), and LiDAR Pulse method  $R^2 = 0.50$ , slope = 0.73,  $p < 0.001$ , RMSE = 0.14**  
 289 **(triangles). Dashed line in panel (a) represents 1:1 relationship. (b) The difference between  $\text{PAI}_{\text{TLS}}$  and  $\text{PAI}_{\text{DHP}}$**   
 290 **estimates for the 2D Intensity Image method, and LiDAR Pulse method. Dashed line at in panel (b)**  
 291 **represents 0). Lines show statistically significant relationships fitted using SMA ( $p < 0.01$ ).**

### 292 3.2 Comparison of whole plot plant area index estimated using TLS and DHP and the effect of plot structure 293 on PAI

294 We found statistically significant correlations between whole plot  $\text{PAI}_{\text{TLS}}$  values and  $\text{PAI}_{\text{DHP}}$   
 295  $\text{PAI}_{\text{DHP}}$  for all three TLS methods (Figure 4). As for single scans (Figure 3), the *LiDAR Pulse* method showed  
 296 the closest agreement to  $\text{PAI}_{\text{DHP}}$ , here compared to both the *Voxel-Based* and *2D Intensity Image*  
 297 methods (SMA; *LiDAR Pulse* method  $R^2 = 0.66$ , slope = 0.82,  $p < 0.01$ , RMSE = 0.14; *Voxel-Based* method  $R^2 =$   
 298  $0.39$ , slope = 2.76,  $p < 0.01$ , RMSE = 0.88; *2D Intensity Image* method  $R^2 = 0.35$ , slope = 0.36,  $p < 0.01$ , RMSE =  
 299  $0.39$ , respectively; Figure 4a). The *2D Intensity Image* method and *LiDAR Pulse* method consistently  
 300 underestimated PAI compared to DHP, whilst the *Voxel-Based* method underestimated in plots with lower  $\text{PAI}_{\text{DHP}}$   
 301  $\text{PAI}_{\text{DHP}}$  and overestimated in plots with higher  $\text{PAI}_{\text{DHP}}$ . The *Voxel-Based* method's high PAI values  
 302 compared to other methods is likely due to its use of multiple co-registered scans reducing occlusion effects  
 303 prevalent in single scan data.

304 To assess the effect of plot structure on variation in TLS derived PAI, we compared  $\text{PAI}_{\text{TLS}}$  estimates to  
 305 TLS estimated crown area index (CAI,  $\text{m}^2$  projected crown area per  $\text{m}^2$  ground area, Figure 4b). We found a  
 306 significant positive relationship between CAI and PAI estimated using each of the *LiDAR Pulse* method, the  
 307 *Voxel-Based* method, and DHP (SMA; *LiDAR Pulse* method  $R^2 = 0.79$ , slope = 1.69,  $p < 0.01$ ; *Voxel-Based* method  
 308  $R^2 = 0.76$ , slope = 5.72,  $p < 0.01$ ; *2D Intensity Image* method  $R^2 = 0.15$ , slope = 0.76,  $p < 0.05$ ; DHP  $R^2 = 0.46$ ,  
 309 slope = 2.07,  $p < 0.01$ , respectively; Figure 4b), where the *2D Intensity Image* method shows signs of appears to  
 310 saturation at medium CAI values (Figure 4b).



311

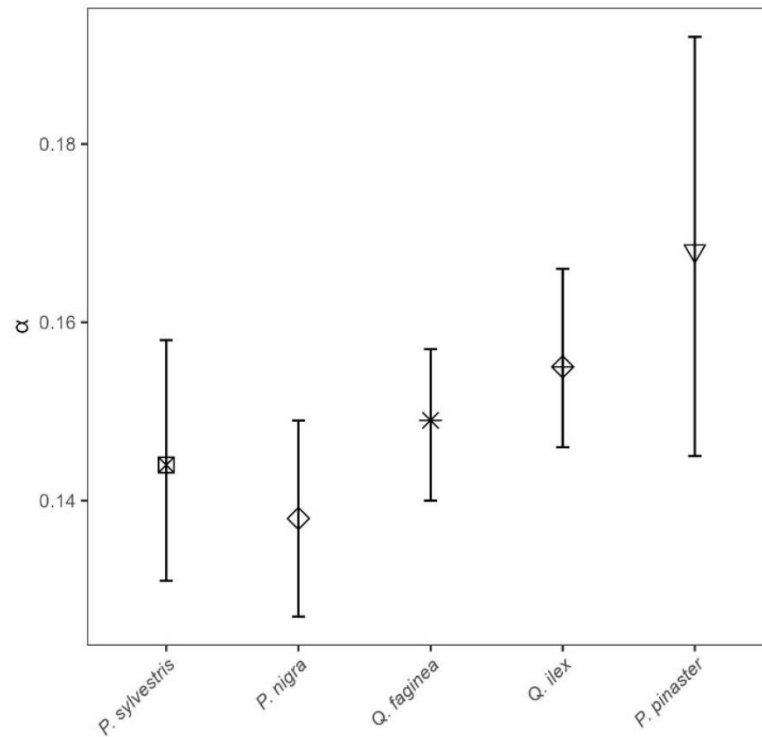
312 **Figure 4: Comparison of plot level  $TLS-PAI$  vs  $DHP-PAI$ , and CAI vs PAI estimates for all 33 plots.**  
 313 **(a) The correlation between DHP derived PAI and PAI derived using 2D Intensity Image  $R^2 = 0.35$ , slope = 0.36,  $p < 0.01$ ,**  
 314  **$RMSE = 0.39$  (circle), LiDAR Pulse  $R^2 = 0.66$ , slope = 0.82,  $p < 0.01$ ,  $RMSE = 0.14$  (triangle) and Voxel-Based  $R^2 = 0.39$ ,**  
 315 **slope = 2.76,  $p < 0.01$ ,  $RMSE = 0.88$  (cross) methods (b) The correlation between TLS derived CAI and PAI derived**  
 316 **using DHP  $R^2 = 0.46$ , slope = 2.07,  $p < 0.01$  (square), 2D Intensity Image  $R^2 = 0.15$ , slope = 0.76,  $p < 0.05$  (circle) LiDAR**  
 317 **Pulse  $R^2 = 0.79$ , slope = 1.69,  $p < 0.01$  (triangle) and Voxel-Based  $R^2 = 0.76$ , slope = 5.72,  $p < 0.01$  (cross) methods. Lines**  
 318 **show statistically significant relationships fitted using SMA ( $p < 0.01$ ). Dashed line in panel (a) represents 1:1**  
 319 **relationship.**

320

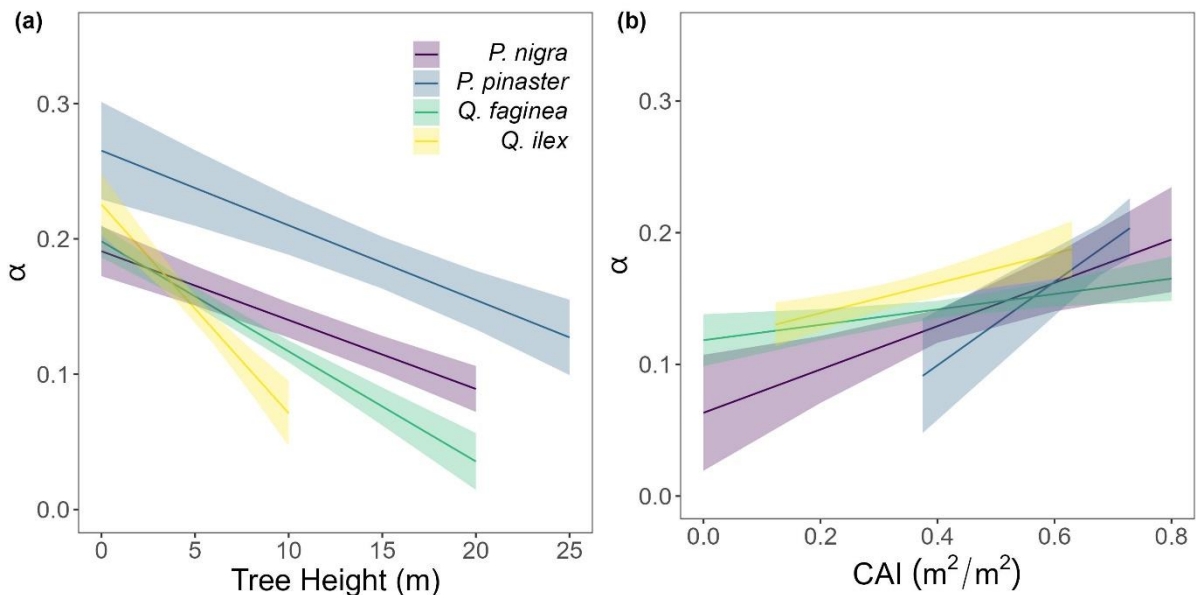
### 321 3.4 Influence of species, tree height and CAI on $\alpha$

322 To understand drivers of variance in  $\alpha$ , we used individual tree PAI and WAI, calculated using the *Voxel-Based*  
 323 method to test the relationship between species and  $\alpha$ , and height/ CAI and  $\alpha$ . We found that more drought tolerant  
 324 species generally had higher  $\alpha$  values than less drought tolerant species (Table BA1; Figure 5), however,  
 325 confidence intervals were wide and overlapping, suggesting that species is not a strong predictor of variation in  
 326  $\alpha$ . We found a statistically significant negative effect of height ( $p < 0.001$ ; Table BA2; Figure 6a) and positive  
 327 effect of CAI ( $p < 0.01 - 0.05$ ; Table BA2; Figure 6b) on  $\alpha$  for all species apart from *P. sylvestris*.  $\alpha$  decreased  
 328 more rapidly with height and increased less rapidly with CAI for oaks than pines. Statistically significant ICC  
 329 values were higher for *P. nigra* (ICC = 0.211; Table BA2) than *P. pinaster*, *Q. faginea* and *Q. ilex* (ICC = 0.036;  
 330 0.060; 0.070, respectively), showing that more  $\alpha$  variation is explained by the random plot effect in *P. nigra* than  
 331 the other species. *P. pinaster* has a wider confidence interval (Figure 5), possibly explained by its lower sample

332 size. [To understand drivers of variance in WAI we carried out additional analysis to test the relationship between](#)  
 333 [WAI and species, height, CAI and PAI, and presented these results in Appendix C \(Figure C3; Tables C3, C4\).](#)



334 **Figure 5: Linear mixed model derived  $\alpha$  values (a, equation 1) for all 2472 individual trees of species *P. sylvestris*, *P.*  
 335 *nigra*, *Q. faginea*, *Q. ilex* and *P. pinaster*. Error bars represent 95% confidence intervals. Species are listed **left to right**  
 336 **from low – high drought tolerance**, with the exception of *P. pinaster*, for which drought tolerance index has not been  
 337 **calculated in the literature. [Drought tolerance rankings are taken from \(Niinemets and Valladares, \(2006\).](#)****



338 **Figure 6: Variation in  $\alpha$  for each species: *Pinus nigra*, *P. pinaster*, *Q. faginea* and *Q. ilex* with (a) height and (b) plot  
 339 **CAI. Lines represent statistically significant linear mixed models (equation 2; [significance levels from  \$p < 0.001\$  to  \$p <\$](#)**   
 340 **[0.05](#)).** Ribbons represent 95% confidence intervals. The model for *P. sylvestris* was not statistically significant.**

341

342

343

## 344 4. Discussion

### 345 4.1 Comparison of approaches to deriving PAI from remote sensed data

346 We found substantial differences in PAI values estimated from TLS and DHP and from different TLS processing  
347 methods (Figures 3 and 4). Further, differences between TLS methods varied across plot structure (CAI), with the  
348 greatest differences between methods in plots with high CAI, and therefore high canopy density. Although  
349 previous studies have presented TLS as an improvement over DHP due to its independence of illumination and  
350 sky conditions during the data acquisition phase, and ability to resolve fine-scale canopy elements and gaps  
351 (Calders et al., 2018; Grotti et al., 2020; Zhu et al., 2018), we have shown that there is large variability between  
352 TLS processing methods in Mediterranean forests. Rigorous intercomparison of approaches, ideally using  
353 standard benchmarking TLS datasets, and destructive sampling, would improve trust and reliability of TLS  
354 algorithms.

### 355 ~~4.2 The LiDAR Pulse and 2D Intensity Image method derived PAI estimates were lower than those derived~~ 356 ~~from DHP and the Voxel-Based method~~

357 We found the *LiDAR Pulse* method (Jupp et al., 2008) to have the best agreement with DHP for both whole plot  
358 and single scan PAI estimates. In contrast to previous ~~studies comparing PAI<sub>TLS</sub> with PAI<sub>DHP</sub> comparisons~~  
359 (Calders et al., 2018; Grotti et al., 2020; Woodgate et al., 2015), we found that the *LiDAR Pulse* and *2D Intensity*  
360 *Image* methods underestimated PAI compared to DHP, except at very low PAI values (~~PAI<sub>TLS</sub> < 0.5~~).  
361 Quantification of PAI from DHP may introduce additional sources of error, for example, its relatively lower  
362 resolution compared to TLS could lead to mixed pixels that have a greater chance of misclassification of sky as  
363 vegetation (Jonckheere et al., 2004). This effect could be enhanced in a Mediterranean forest as trees in drier  
364 climates tend to have smaller leaves (Peppe et al., 2011), leading to more small canopy gaps that TLS may resolve  
365 where DHP cannot. Further, although we took steps to reduce the error introduced at DHP data acquisition and  
366 processing steps, including using automatic thresholding and collecting images with multiple exposures, DHP  
367 processing requires both model and user assumptions that can impact results. For example, ~~DHP-PAI/PAI<sub>DHP</sub>~~  
368 estimates are highly sensitive to camera exposure; increasing one stop of exposure can result in 3 – 28% difference  
369 in PAI and use of automatic exposure can result in up to 70% error (Zhang et al., 2005).

370 We found the *Voxel-Based* method overestimated PAI values compared to the other methods at the whole plot  
371 level. This is likely due to the method's use of co-registered scans, rather than averaged single scan PAI values,  
372 since co-registered scans will reduce occlusion effects prevalent in single scan data that could lead to an  
373 underestimation of PAI (Wilkes et al., 2017). The *Voxel-Based* method is, however, sensitive to voxel size (Li et  
374 al., 2016), and larger voxels lead to larger PAI estimates as they fill small canopy gaps; we chose a voxel size of  
375 0.05 m to match the minimum distance between points in our downsampled dataset. However, the *Voxel-Based*  
376 method is a memory intensive approach to calculating PAI, and smaller voxels have higher memory requirements.  
377 We picked this data resolution, and therefore voxel size, to balance the need to capture fine-scale canopy details  
378 against memory requirements for running ~~the method on~~ many large plot ~~point clouds~~. Voxel size could have  
379 been chosen based on estimates' match to DHP, but this would assume (1) that DHP estimates are most accurate,  
380 and (2) that DHP data are always available, limiting the wider applicability of our findings. Understanding which  
381 method is over- or underestimating would require a destructively sampled dataset for validation, which was not



382 possible for this study (or most ecosystems). However, other studies using voxel approaches have found that  
383 although these produce high LAI values for individual trees, these are underestimates compared with destructive  
384 samples (Li et al., 2016). Regardless, PAI and LAI estimates using a *Voxel-Based* approach are highly dependent  
385 on voxel size (~~Béland et al., 2014~~) (Li et al., 2016), and future work should test the influence of voxel size on PAI  
386 estimates, using destructive samples in a range of environments.

#### 387 **4.3 Relationship between PAI and CAI varied according to method and sensor**

388 The relationship between the LiDAR Pulse method had the strongest relationship (defined as highest  $R^2$ ) with and  
389 TLS derived CAI had the highest  $R^2$ , demonstrating that the method is well suited to measuring PAI across the  
390 range of plot CAI values used in this study. Although the *2D Intensity Image* method can tackle the significant  
391 challenges presented by edge effects and partial beam interceptions, particularly present in phase-shift systems  
392 (Grotti et al., 2020), our results suggest this method has a lower performance ability, with saturation occurring  
393 sooner than all other methods in dense forests (Figures 3 and 4). The *2D Intensity Image* method uses the same  
394 raw single scan data as the *LiDAR Pulse* method, so the better performance from the latter is likely due to the  
395 method's use of vertically resolved gap fraction; both the *LiDAR Pulse* method and *Voxel-Based* method account  
396 for the vertical structure of the canopy by summing vertical slices through the canopy.

#### 397 **4.24 $\alpha$ variation between species and plot**

398 We used the *Voxel-Based* method to investigate individual tree  $\alpha$  variation between species and across structure,  
399 as this was the only approach we compared identified that could be applied to single tree point clouds which are  
400 leaf-wood separated. We found  $\alpha$  values obtained were within the range of values obtained from destructive  
401 approaches (0.1 – 0.6, Gower et al., 1997). The drought and shade intolerant *P. nigra* showed stronger variability  
402 in  $\alpha$  across plots (higher ICC value, Table BA2) than other species, suggesting its wood – leaf ratio may be more  
403 sensitive to site factors. However, as the plots measured in this study vary in both abiotic conditions (altitude,  
404 aspect, slope, wetness) as well as species composition, stem density and canopy cover, there may be other drivers  
405 of variation in  $\alpha$  values.

406 We found some evidence that species with higher drought tolerance had higher  $\alpha$  values (Figure 5; Table BA1),  
407 however, confidence intervals were wide, suggesting a weak relationship. There is evidence that trees that tolerate  
408 water limited environments have a lower leaf area (Battaglia et al., 1998; Mencuccini and Grace, 1995), so higher  
409  $\alpha$  values may reflect maintenance of homeostasis of leaf water use through adjustment of wood to leaf area ratio  
410 (Carter and White, 2009; Gazal et al., 2006). The potential for a tree to lose water is mostly regulated through leaf  
411 traits including stomatal conductance and leaf area, and both stand (Battaglia et al., 1998; Specht and Specht,  
412 1989) and individual tree (Mencuccini, 2003) water use have been found to scale linearly with LAI, with drought  
413 often mitigated through leaf shedding (López et al., 2021).

#### 414 **4.35 Tree stature and stand density drives $\alpha$ variation**

415 Although species had a weak relationship with explain some variation in  $\alpha$ , tree height and plot CAI were stronger  
416 predictorshad a statistically significant relationship with  $\alpha$  ( $p < 0.001$  –  $p < 0.05$ ) for all species, showing the  
417 importance of local stand structure on leaf and woody allocation. We found that  $\alpha$  scaled negatively with height  
418 for all species apart from *P. sylvestris*, suggesting that in this environment, taller trees generally have a lower  
419 proportion of wood to plant area index than shorter ones. *P. sylvestris*, which is at the edge of its geographical

420 range and physiological limits (Castro-Díez et al., 1997; Owen et al., 2021), showed no significant relationship  
421 between height and  $\alpha$ . We found that  $\alpha$  scaled positively with plot level CAI for all species apart from *P. sylvestris*,  
422 that is, trees growing in denser plots have a higher  $\alpha$ . This supports theory that trees growing in dense forests are  
423 competing for resources, reducing individual tree leaf area (Jump et al., 2017). The negative height –  $\alpha$  and positive  
424 CAI –  $\alpha$  relationships in our model suggest that trees may initially invest in vertical growth to reach the canopy  
425 level, and once there invest in lateral growth, with more leaf area, to increase light capture. This supports theory  
426 that trees grow to outcompete neighbouring individuals for light capture (Purves and Pacala, 2008) and evidence  
427 that both lateral growth and LAI are reduced beneath closed canopies (Beaudet and Messier, 1998; Canham,  
428 1988).

429 Wood may be harder to accurately classify than leaves in TLS data (Vicari et al., 2019), resulting in a higher  
430 occurrence of false positives in wood clouds, potentially leading to an overestimation in WAI, and therefore  
431 underestimation of  $\alpha$ , especially in trees with small leaves which are prevalent in dry, Mediterranean environments  
432 (Peppe et al., 2011). The problem of misclassification will increase in taller trees due to TLS beam divergence,  
433 occlusion and larger beam footprint at further distances (Vicari et al., 2019), suggesting that WAI overestimation  
434 could be more pronounced in tall trees. Although our dense scanning strategy (Owen et al., 2021) was designed  
435 to mitigate some of these effects, these effects mean it is possible our findings may could underestimate the slope  
436 of the negative relationship between  $\alpha$  and tree height.

#### 437 **4.46 Correcting for non-photosynthetic elements in LAI estimates using TLS**

438 The value of TLS data to estimate individual tree PAI, WAI and subsequently  $\alpha$ , demonstrates their potential to  
439 corrective factors for non-photosynthetic components in ground based remote sensing measurements of LAI.  
440 Properly correcting for WAI in LAI estimates is of global importance as small errors in ground based  
441 measurements propagate through to large scale satellite observations generating large errors in global vegetation  
442 models (Calders et al., 2018). The work presented here provides a foundation for future work combining multi-  
443 source and multi-scale remote sensing datasets to correct large-scale LAI products. Our results echo others' in  
444 finding that the prevalence of woody material in the tree canopy, and therefore  $\alpha$ , is dynamic and varies by species  
445 as well as senescence, crown health and, in the case of deciduous forests, leaf phenology (Gower et al., 1999).  
446 The use of single  $\alpha$  value in a plot or region (Olivas et al., 2013; Woodgate et al., 2016), invariant of species, size  
447 and forest structure, to convert PAI to LAI is therefore problematic (Niu et al., 2021). Our study demonstrates the  
448 importance of taking species mix and structural variation into account when correcting for non-photosynthetic  
449 material in ground-based LAI estimates.

#### 450 **5. Conclusions**

451 We tested three methods for estimating PAI using Terrestrial Laser Scanning data and compared these against  
452 traditional DHP measurements. We found large variation between PAI values estimated from each TLS method  
453 and DHP, demonstrating that care should be taken when deriving PAI from ground based remote sensing methods.  
454 Although the *LiDAR Pulse* method was found to have the best agreement with both single scan and whole plot  
455 PAI values measured by DHP, the *Voxel-Based* method allowed separate analysis of the key metric used to correct  
456 for the effect of WAI in LAI measurements,  $\alpha$ , in individual trees. We recommend the *LiDAR Pulse* method as a  
457 fast and effective method for PAI estimation independent of illumination conditions. Whilst the *Voxel-Based*

458 method may be used to analyse individual tree  $\alpha$  and determine ecological drivers of variation, work remains to  
459 determine the validity of these approaches, in particular correct voxel size choice. We found that  $\alpha$  varies by  
460 species, height and stand density, showing the importance of accurately correcting for WAI on the individual tree  
461 level and the utility of TLS to do so.

462 The variation in our results for the different methods used to derive PAI from TLS data show that there is some  
463 way to go before TLS derived vegetation indices can be interpreted as robust and reliable. Validation using  
464 destructive samples and further intercomparison studies of methods are needed to demonstrate the advantages of  
465 TLS, and use of benchmarking datasets should be standard. DHP is a faster, cheaper and more widely accessible  
466 method for PAI estimation, and while TLS promises to alleviate potential bias in DHP estimates, results are highly  
467 methods dependent. Our results demonstrate the challenges that stand in the way of large scale adoption of TLS  
468 for vegetation indices monitoring.

## 469 **6. Code availability**

470 See [https://github.com/will-flynn/tls\\_dhp\\_pai.git](https://github.com/will-flynn/tls_dhp_pai.git) for all processing and modelling code.

## 471 **7. Data availability**

472 See Owen et al., (2022) for individual segmented tree data [and](#) (Flynn et al., (2023) [for thresholded DHP](#)  
473 [images](#).

## 474 **8. Author contribution**

475 All authors designed the study. HJFO and WRMF collected and processed TLS and DHP data; WRMF performed  
476 formal analysis with guidance from all authors. WRMF led the writing with input from all authors. All authors  
477 contributed critically to drafts and gave final approval for publication.

## 478 **9. Competing interests**

479 The authors declare that they have no conflict of interest.

## 480 **7. Acknowledgements**

481 WRMF was funded through a London NERC DTP PhD studentship. ERL, HJFO and SWDG were funded through  
482 the UKRI Future Leaders Fellowship awarded to ERL (MR/T019832/1).

## 483 **References**

484 Baeten, L., Verheyen, K., Wirth, C., Bruelheide, H., Bussotti, F., Finér, L., Jaroszewicz, B., Selvi, F.,  
485 Valladares, F., Allan, E., Ampoorter, E., Auge, H., Avăcăriei, D., Barbaro, L., Bărnoaiea, I., Bastias, C. C.,  
486 Bauhus, J., Beinhoff, C., Benavides, R., Benneter, A., Berger, S., Berthold, F., Boberg, J., Bonal, D.,  
487 Brüggemann, W., Carnol, M., Castagneyrol, B., Charbonnier, Y., Čečko, E., Coomes, D., Coppi, A., Dalmaris,  
488 E., Dănilă, G., Dawud, S. M., de Vries, W., De Wandeler, H., Deconchat, M., Domisch, T., Duduman, G.,  
489 Fischer, M., Fotelli, M., Gessler, A., Gimeno, T. E., Granier, A., Grossiord, C., Guyot, V., Hantsch, L.,  
490 Hättenschwiler, S., Hector, A., Hermy, M., Holland, V., Jactel, H., Joly, F.-X., Jucker, T., Kolb, S., Koricheva,  
491 J., Lexer, M. J., Liebergesell, M., Milligan, H., Müller, S., Muys, B., Nguyen, D., Nichiforel, L., Pollastrini, M.,  
492 Proulx, R., Rabasa, S., Radoglou, K., Ratcliffe, S., Raulund-Rasmussen, K., Seiferling, I., Stenlid, J., Vesterdal,  
493 L., von Wilpert, K., Zavala, M. A., Zielinski, D., and Scherer-Lorenzen, M.: A novel comparative research  
494 platform designed to determine the functional significance of tree species diversity in European forests,  
495 *Persepect. Plant. Ecol.*, 15, 281–291, <https://doi.org/10.1016/j.ppees.2013.07.002>, 2013.

496 Baret, F., Weiss, M., Lacaze, R., Camacho, F., Makhmara, H., Pacholczyk, P., and Smets, B.: GEOV1: LAI and  
497 FAPAR essential climate variables and FCOVER global time series capitalizing over existing products. Part1:

- 498 Principles of development and production, *Remote Sens. Environ.*, 137, 299–309,  
499 <https://doi.org/10.1016/j.rse.2012.12.027>, 2013.
- 500 Bates, D., Mächler, M., Bolker, B., and Walker, S.: Fitting Linear Mixed-Effects Models Using lme4, *J. Stat.*  
501 *Softw.*, 67, <https://doi.org/10.18637/jss.v067.i01>, 2015.
- 502 Battaglia, M., Cherry, M. L., Beadle, C. L., Sands, P. J., and Hingston, A.: Prediction of leaf area index in  
503 eucalypt plantations: effects of water stress and temperature, *Tree Physiol.*, 18, 521–528,  
504 <https://doi.org/10.1093/treephys/18.8-9.521>, 1998.
- 505 Beaudet, M. and Messier, C.: Growth and morphological responses of yellow birch, sugar maple, and beech  
506 seedlings growing under a natural light gradient, *Can. J. Forest Res.*, 28, 1007–1015,  
507 <https://doi.org/10.1139/x98-077>, 1998.
- 508 Béland, M., Baldocchi, D. D., Widlowski, J.-L., Fournier, R. A., and Verstraete, M. M.: On seeing the wood  
509 from the leaves and the role of voxel size in determining leaf area distribution of forests with terrestrial LiDAR,  
510 *Agr. Forest Meteorol.*, 184, 82–97, <https://doi.org/10.1016/j.agrformet.2013.09.005>, 2014.
- 511 Breda, N. J. J.: Ground-based measurements of leaf area index: a review of methods, instruments and current  
512 controversies, *J. Exp. Bot.*, 54, 2403–2417, <https://doi.org/10.1093/jxb/erg263>, 2003.
- 513 Burt, A., Disney, M., and Calders, K.: Extracting individual trees from lidar point clouds using treeSeg, *Methods*  
514 *Ecol. Evol.*, 10, 438–445, <https://doi.org/10.1111/2041-210X.13121>, 2019.
- 515 Calders, K., Armston, J., Newnham, G., Herold, M., and Goodwin, N.: Implications of sensor configuration and  
516 topography on vertical plant profiles derived from terrestrial LiDAR, *Agr. Forest Meteorol.*, 194, 104–117,  
517 <https://doi.org/10.1016/j.agrformet.2014.03.022>, 2014.
- 518 Calders, K., Origo, N., Disney, M., Nightingale, J., Woodgate, W., Armston, J., and Lewis, P.: Variability and  
519 bias in active and passive ground-based measurements of effective plant, wood and leaf area index, *Agr. Forest*  
520 *Meteorol.*, 252, 231–240, <https://doi.org/10.1016/j.agrformet.2018.01.029>, 2018.
- 521 Calders, K., Adams, J., Armston, J., Bartholomeus, H., Bauwens, S., Bentley, L. P., Chave, J., Danson, F. M.,  
522 Demol, M., Disney, M., Gaulton, R., Krishna Moorthy, S. M., Levick, S. R., Saarinen, N., Schaaf, C., Stovall,  
523 A., Terryn, L., Wilkes, P., and Verbeeck, H.: Terrestrial laser scanning in forest ecology: Expanding the  
524 horizon, *Remote Sensing of Environment*, 251, 112102, <https://doi.org/10.1016/j.rse.2020.112102>, 2020.
- 525 Canham, C. D.: Growth and Canopy Architecture of Shade-Tolerant Trees: Response to Canopy Gaps, *Ecology*,  
526 69, 786–795, <https://doi.org/10.2307/1941027>, 1988.
- 527 Carter, J. L. and White, D. A.: Plasticity in the Huber value contributes to homeostasis in leaf water relations of  
528 a mallee Eucalypt with variation to groundwater depth, *Tree Physiol.*, 29, 1407–1418,  
529 <https://doi.org/10.1093/treephys/tpp076>, 2009.
- 530 Caspersen, J. P., Vanderwel, M. C., Cole, W. G., and Purves, D. W.: How Stand Productivity Results from Size-  
531 and Competition-Dependent Growth and Mortality, *PLoS ONE*, 6, e28660,  
532 <https://doi.org/10.1371/journal.pone.0028660>, 2011.
- 533 Castro-Díez, P., Villar-Salvador, P., Pérez-Rantomé, C., Maestro-Martínez, M., and Montserrat-Martí, G.: Leaf  
534 morphology and leaf chemical composition in three *Quercus* (Fagaceae) species along a rainfall gradient in NE  
535 Spain, *Trees*, 11, 127–134, <https://doi.org/10.1007/PL00009662>, 1997.
- 536 Chen, J. M. and Black, T. A.: Defining leaf area index for non-flat leaves, *Plant Cell Environ.*, 15, 421–429,  
537 <https://doi.org/10.1111/j.1365-3040.1992.tb00992.x>, 1992.
- 538 Coomes, D. A., Holdaway, R. J., Kobe, R. K., Lines, E. R., and Allen, R. B.: A general integrative framework  
539 for modelling woody biomass production and carbon sequestration rates in forests, *Journal of Ecology*, 100, 42–  
540 64, <https://doi.org/10.1111/j.1365-2745.2011.01920.x>, 2012.

- 541 Disney, M.: Terrestrial LiDAR: a three-dimensional revolution in how we look at trees, *New Phytol.*, 222,  
542 1736–1741, <https://doi.org/10.1111/nph.15517>, 2018.
- 543 Flynn, W. R. M., Owen, H. J. F., Grieve, S. W. D., and Lines, E. R.: DHP images collected from Alto Tajo and  
544 Cuellar in Spain. (V1), <https://doi.org/10.5281/ZENODO.7628072>, 2023.
- 545 Gazal, R. M., Scott, R. L., Goodrich, D. C., and Williams, D. G.: Controls on transpiration in a semiarid riparian  
546 cottonwood forest, *Agr. Forest Meteorol.*, 137, 56–67, <https://doi.org/10.1016/j.agrformet.2006.03.002>, 2006.
- 547 Gower, S. T., Vogel, J. G., Norman, J. M., Kucharik, C. J., Steele, S. J., and Stow, T. K.: Carbon distribution  
548 and aboveground net primary production in aspen, jack pine, and black spruce stands in Saskatchewan and  
549 Manitoba, Canada, *J. Geophys. Res.*, 102, 29029–29041, <https://doi.org/10.1029/97JD02317>, 1997.
- 550 Gower, S. T., Kucharik, C. J., and Norman, J. M.: Direct and Indirect Estimation of Leaf Area Index, fAPAR,  
551 and Net Primary Production of Terrestrial Ecosystems, *Remote Sens. Environ.*, 70, 29–51,  
552 [https://doi.org/10.1016/S0034-4257\(99\)00056-5](https://doi.org/10.1016/S0034-4257(99)00056-5), 1999.
- 553 Grotti, M., Calders, K., Origo, N., Puletti, N., Alivernini, A., Ferrara, C., and Chianucci, F.: An intensity, image-  
554 based method to estimate gap fraction, canopy openness and effective leaf area index from phase-shift terrestrial  
555 laser scanning, *Agr. Forest Meteorol.*, 280, 107766, <https://doi.org/10.1016/j.agrformet.2019.107766>, 2020.
- 556 Hardwick, S. R., Toumi, R., Pfeifer, M., Turner, E. C., Nilus, R., and Ewers, R. M.: The relationship between  
557 leaf area index and microclimate in tropical forest and oil palm plantation: Forest disturbance drives changes in  
558 microclimate, *Agr. Forest Meteorol.*, 201, 187–195, <https://doi.org/10.1016/j.agrformet.2014.11.010>, 2015.
- 559 Hijmans, R. J.: raster: Geographic Data Analysis and Modeling R package version 3.5-21, [https://CRAN.R-](https://CRAN.R-project.org/package=raster)  
560 [project.org/package=raster.](https://CRAN.R-project.org/package=raster), 2022.
- 561 Hosoi, F. and Omasa, K.: Voxel-Based 3-D Modeling of Individual Trees for Estimating Leaf Area Density  
562 Using High-Resolution Portable Scanning Lidar, *IEEE T. Geosci. Remote*, 44, 3610–3618,  
563 <https://doi.org/10.1109/TGRS.2006.881743>, 2006.
- 564 Itakura, K. and Hosoi, F.: Voxel-based leaf area estimation from three-dimensional plant images, *J. Agric.*  
565 *Meteorol.*, 75, 211–216, <https://doi.org/10.2480/agrmet.d-19-00013>, 2019.
- 566 Jonckheere, I., Fleck, S., Nackaerts, K., Muys, B., Coppin, P., Weiss, M., and Baret, F.: Review of methods for  
567 in situ leaf area index determination, *Agr. Forest Meteorol.*, 121, 19–35,  
568 <https://doi.org/10.1016/j.agrformet.2003.08.027>, 2004.
- 569 Jonckheere, I. G. C., Muys, B., and Coppin, P.: Allometry and evaluation of in situ optical LAI determination in  
570 Scots pine: a case study in Belgium, *Tree Physiol.*, 25, 723–732, <https://doi.org/10.1093/treephys/25.6.723>,  
571 2005.
- 572 Jucker, T., Bouriaud, O., Avacaritei, D., Dănilă, I., Duduman, G., Valladares, F., and Coomes, D. A.:  
573 Competition for light and water play contrasting roles in driving diversity-productivity relationships in Iberian  
574 forests, *J. Ecol.*, 102, 1202–1213, <https://doi.org/10.1111/1365-2745.12276>, 2014.
- 575 Jump, A. S., Ruiz-Benito, P., Greenwood, S., Allen, C. D., Kitzberger, T., Fensham, R., Martínez-Vilalta, J.,  
576 and Lloret, F.: Structural overshoot of tree growth with climate variability and the global spectrum of drought-  
577 induced forest dieback, *Glob. Change Biol.*, 23, 3742–3757, <https://doi.org/10.1111/gcb.13636>, 2017.
- 578 Jupp, D. L. B., Culvenor, D. S., Lovell, J. L., Newnham, G. J., Strahler, A. H., and Woodcock, C. E.: Estimating  
579 forest LAI profiles and structural parameters using a ground-based laser called 'Echidna(R)', *Tree Physiol.*, 29,  
580 171–181, <https://doi.org/10.1093/treephys/tpn022>, 2008.
- 581 Kamoske, A. G., Dahlin, K. M., Stark, S. C., and Serbin, S. P.: Leaf area density from airborne LiDAR:  
582 Comparing sensors and resolutions in a temperate broadleaf forest ecosystem, *Forest Ecol. Manag.*, 433, 364–  
583 375, <https://doi.org/10.1016/j.foreco.2018.11.017>, 2019.



- 584 Kuusk, V., Niinemets, Ü., and Valladares, F.: A major trade-off between structural and photosynthetic  
585 investments operative across plant and needle ages in three Mediterranean pines, *Tree Physiol.*, 38, 543–557,  
586 <https://doi.org/10.1093/treephys/tpx139>, 2018.
- 587 Leblanc, S. G. and Chen, J. M.: A practical scheme for correcting multiple scattering effects on optical LAI  
588 measurements, *Agr. Forest Meteorol.*, 110, 125–139, [https://doi.org/10.1016/S0168-1923\(01\)00284-2](https://doi.org/10.1016/S0168-1923(01)00284-2), 2001.
- 589 Lecigne, B., Delagrangé, S., and Messier, C.: Exploring trees in three dimensions: VoxR, a novel voxel-based R  
590 package dedicated to analysing the complex arrangement of tree crowns, *Ann. Bot-London*, 121, 589–601,  
591 <https://doi.org/10.1093/aob/mcx095>, 2018.
- 592 Li, S., Dai, L., Wang, H., Wang, Y., He, Z., and Lin, S.: Estimating Leaf Area Density of Individual Trees  
593 Using the Point Cloud Segmentation of Terrestrial LiDAR Data and a Voxel-Based Model, *Remote Sens-Basel*,  
594 9, 1202, <https://doi.org/10.3390/rs9111202>, 2017.
- 595 Li, Y., Guo, Q., Tao, S., Zheng, G., Zhao, K., Xue, B., and Su, Y.: Derivation, Validation, and Sensitivity  
596 Analysis of Terrestrial Laser Scanning-Based Leaf Area Index, *Can. J. Remote Sens.*, 42, 719–729,  
597 <https://doi.org/10.1080/07038992.2016.1220829>, 2016.
- 598 Lines, E. R., Fischer, F. J., Owen, H. J. F., and Jucker, T.: The shape of trees: Reimagining forest ecology in  
599 three dimensions with remote sensing, *J. Ecol.*, 110, 1730–1745, <https://doi.org/10.1111/1365-2745.13944>,  
600 2022.
- 601 Long, J. N. and Smith, F. W.: Leaf area - sapwood area relations of lodgepole pine as influenced by stand  
602 density and site index., *Can. J. Forest Res.*, 18, 247–250, 1988.
- 603 López, R., Cano, F. J., Martin-StPaul, N. K., Cochard, H., and Choat, B.: Coordination of stem and leaf traits  
604 define different strategies to regulate water loss and tolerance ranges to aridity, *New Phytol.*, 230, 497–509,  
605 <https://doi.org/10.1111/nph.17185>, 2021.
- 606 Lovell, J. L., Jupp, D. L. B., van Gersel, E., Jimenez-Berni, J., Hopkinson, C., and Chasmer, L.: Foliage Profiles  
607 from Ground Based Waveform and Discrete Point Lidar, *SilviLaser*, 1–9, 2011.
- 608 Ma, L., Zheng, G., Eitel, J. U. H., Magney, T. S., and Moskal, L. M.: Determining woody-to-total area ratio  
609 using terrestrial laser scanning (TLS), *Agr. Forest Meteorol.*, 228–229, 217–228,  
610 <https://doi.org/10.1016/j.agrformet.2016.06.021>, 2016.
- 611 Madrigal-González, J., Herrero, A., Ruiz-Benito, P., and Zavala, M. A.: Resilience to drought in a dry forest:  
612 Insights from demographic rates, *Forest Ecol. Manag.*, 389, 167–175,  
613 <https://doi.org/10.1016/j.foreco.2016.12.012>, 2017.
- 614 Magnani, F., Mencuccini, M., and Grace, J.: Age-related decline in stand productivity: the role of structural  
615 acclimation under hydraulic constraints, *Plant Cell Environ.*, 23, 251–263, <https://doi.org/10.1046/j.1365-3040.2000.00537.x>, 2000.
- 617 Mencuccini, M.: The ecological significance of long-distance water transport: short-term regulation, long-term  
618 acclimation and the hydraulic costs of stature across plant life forms, *Plant Cell Environ.*, 26, 163–182,  
619 <https://doi.org/10.1046/j.1365-3040.2003.00991.x>, 2003.
- 620 Mencuccini, M. and Grace, J.: Climate influences the leaf area/sapwood area ratio in Scots pine, *Tree Physiol.*,  
621 15, 1–10, <https://doi.org/10.1093/treephys/15.1.1>, 1995.
- 622 Monsi, M. and Saeki, T.: On the Factor Light in Plant Communities and its Importance for Matter Production,  
623 *Ann. Bot-London*, 95, 549–567, <https://doi.org/10.1093/aob/mci052>, 1953.
- 624 Nakagawa, S., Johnson, P. C. D., and Schielzeth, H.: The coefficient of determination R<sup>2</sup> and intra-class  
625 correlation coefficient from generalized linear mixed-effects models revisited and expanded, *J. R. Soc.*  
626 *Interface*, 14, 20170213, <https://doi.org/10.1098/rsif.2017.0213>, 2017.

627 Niinemets, Ü. and Valladares, F.: Tolerance to shade, drought, and waterlogging of temperate northern  
628 hemisphere trees and shrubs, *Ecol. Monogr.*, 76, 521–547, [https://doi.org/10.1890/0012-](https://doi.org/10.1890/0012-9615(2006)076[0521:TTSDAW]2.0.CO;2)  
629 9615(2006)076[0521:TTSDAW]2.0.CO;2, 2006.

630 Niu, X., Fan, J., Luo, R., Fu, W., Yuan, H., and Du, M.: Continuous estimation of leaf area index and the  
631 woody-to-total area ratio of two deciduous shrub canopies using fisheye webcams in a semiarid loessial region  
632 of China, *Ecol. Indic.*, 125, 107549, <https://doi.org/10.1016/j.ecolind.2021.107549>, 2021.

633 Olivas, P. C., Oberbauer, S. F., Clark, D. B., Clark, D. A., Ryan, M. G., O'Brien, J. J., and Ordoñez, H.:  
634 Comparison of direct and indirect methods for assessing leaf area index across a tropical rain forest landscape,  
635 *Agr. Forest Meterol.*, 177, 110–116, <https://doi.org/10.1016/j.agrformet.2013.04.010>, 2013.

636 Owen, H. J. F., Flynn, W. R. M., and Lines, E. R.: Competitive drivers of inter-specific deviations of crown  
637 morphology from theoretical predictions measured with Terrestrial Laser Scanning, *J. Ecol.*, 109, 2612–2628,  
638 <https://doi.org/10.1111/1365-2745.13670>, 2021.

639 Owen, H. J. F., Flynn, W. R. M., and Lines, E. R.: Individual TLS tree clouds collected from both Alto Tajo and  
640 Cuellar in Spain., 2022.

641 Peppe, D. J., Royer, D. L., Cariglino, B., Oliver, S. Y., Newman, S., Leight, E., Enikolopov, G., Fernandez-  
642 Burgos, M., Herrera, F., Adams, J. M., Correa, E., Currano, E. D., Erickson, J. M., Hinojosa, L. F., Hoganson, J.  
643 W., Iglesias, A., Jaramillo, C. A., Johnson, K. R., Jordan, G. J., Kraft, N. J. B., Lovelock, E. C., Lusk, C. H.,  
644 Niinemets, Ü., Peñuelas, J., Rapson, G., Wing, S. L., and Wright, I. J.: Sensitivity of leaf size and shape to  
645 climate: global patterns and paleoclimatic applications, *New Phytol.*, 190, 724–739,  
646 <https://doi.org/10.1111/j.1469-8137.2010.03615.x>, 2011.

647 Pfeifer, M., Gonsamo, A., Disney, M., Pellikka, P., and Marchant, R.: Leaf area index for biomes of the Eastern  
648 Arc Mountains: Landsat and SPOT observations along precipitation and altitude gradients, *Remote Sens.*  
649 *Environ.*, 118, 103–115, <https://doi.org/10.1016/j.rse.2011.11.009>, 2012.

650 Phillips, N., Bond, B. J., McDowell, N. G., Ryan, M. G., and Schauer, A.: Leaf area compounds height-related  
651 hydraulic costs of water transport in Oregon White Oak trees, *Funct. Ecol.*, 17, 832–840,  
652 <https://doi.org/10.1111/j.1365-2435.2003.00791.x>, 2003.

653 Purves, D. and Pacala, S.: Predictive Models of Forest Dynamics, *Science*, 320, 1452–1453,  
654 <https://doi.org/10.1126/science.1155359>, 2008.

655 Ridler, T. W. and Calvard, S.: Picture Thresholding Using an Iterative Selection Method, *IEEE T. Syst. Man.*  
656 *Cyb.*, 8, 630–632, <https://doi.org/10.1109/TSMC.1978.4310039>, 1978.

657 Sea, W. B., Choler, P., Beringer, J., Weinmann, R. A., Hutley, L. B., and Leuning, R.: Documenting  
658 improvement in leaf area index estimates from MODIS using hemispherical photos for Australian savannas,  
659 *Agr. Forest Meterol.*, 151, 1453–1461, <https://doi.org/10.1016/j.agrformet.2010.12.006>, 2011.

660 Specht, R. L. and Specht, A.: Canopy structure in Eucalyptus-dominated communities in Australia along  
661 climatic gradients, *Canopy structure in Eucalyptus-dominated communities in Australia along climatic*  
662 *gradients*, 10, 191–213, 1989.

663 Vicari, M. B., Disney, M., Wilkes, P., Burt, A., Calders, K., and Woodgate, W.: Leaf and wood classification  
664 framework for terrestrial LiDAR point clouds, *Methods Ecol. Evol.*, 10, 680–694, [https://doi.org/10.1111/2041-](https://doi.org/10.1111/2041-210X.13144)  
665 210X.13144, 2019.

666 Warton, D. I., Wright, I. J., Falster, D. S., and Westoby, M.: Bivariate line-fitting methods for allometry, *Biol.*  
667 *Rev.*, 81, 259–291, <https://doi.org/10.1017/S1464793106007007>, 2006.

668 Warton, D. I., Duursma, R. A., Falster, D. S., and Taskinen, S.: smatr 3 - an R package for estimation and  
669 inference about allometric lines: *The smatr 3 - an R package*, *Methods Ecol. Evol.*, 3, 257–259,  
670 <https://doi.org/10.1111/j.2041-210X.2011.00153.x>, 2012.

- 671 Weiss, M., Baret, F., Smith, G. J., Jonckheere, I., and Coppin, P.: Review of methods for in situ leaf area index  
672 (LAI) determination, *Agr. Forest Meterol.*, 121, 37–53, <https://doi.org/10.1016/j.agrformet.2003.08.001>, 2004.
- 673 Whitehead, D.: The Estimation of Foliage Area from Sapwood Basal Area in Scots Pine, *Forestry*, 51, 137–149,  
674 <https://doi.org/10.1093/forestry/51.2.137>, 1978.
- 675 Wilkes, P., Lau, A., Disney, M., Calders, K., Burt, A., Gonzalez de Tanago, J., Bartholomeus, H., Brede, B., and  
676 Herold, M.: Data acquisition considerations for Terrestrial Laser Scanning of forest plots, *Remote Sensing of*  
677 *Environment*, 196, 140–153, <https://doi.org/10.1016/j.rse.2017.04.030>, 2017.
- 678 Woodgate, W., Jones, S. D., Suarez, L., Hill, M. J., Armston, J. D., Wilkes, P., Soto-Berelev, M., Haywood, A.,  
679 and Mellor, A.: Understanding the variability in ground-based methods for retrieving canopy openness, gap  
680 fraction, and leaf area index in diverse forest systems, *Agr. Forest Meterol.*, 205, 83–95,  
681 <https://doi.org/10.1016/j.agrformet.2015.02.012>, 2015.
- 682 Woodgate, W., Armston, J. D., Disney, M., Jones, S. D., Suarez, L., Hill, M. J., Wilkes, P., and Soto-Berelev,  
683 M.: Quantifying the impact of woody material on leaf area index estimation from hemispherical photography  
684 using 3D canopy simulations, *Agr. Forest Meterol.*, 226–227, 1–12,  
685 <https://doi.org/10.1016/j.agrformet.2016.05.009>, 2016.
- 686 Zhang, Y., Chen, J. M., and Miller, J. R.: Determining digital hemispherical photograph exposure for leaf area  
687 index estimation, *Agr. Forest Meterol.*, 133, 166–181, <https://doi.org/10.1016/j.agrformet.2005.09.009>, 2005.
- 688 Zheng, G., Moskal, L. M., and Kim, S.-H.: Retrieval of Effective Leaf Area Index in Heterogeneous Forests  
689 With Terrestrial Laser Scanning, *IEEE T. Geosci. Remote*, 51, 777–786,  
690 <https://doi.org/10.1109/TGRS.2012.2205003>, 2013.
- 691 Zhu, X., Skidmore, A. K., Wang, T., Liu, J., Darvishzadeh, R., Shi, Y., Premier, J., and Heurich, M.: Improving  
692 leaf area index (LAI) estimation by correcting for clumping and woody effects using terrestrial laser scanning,  
693 *Agr. Forest Meterol.*, 263, 276–286, <https://doi.org/10.1016/j.agrformet.2018.08.026>, 2018.
- 694